Interstitial Occupancy by Extrinsic Alkali Cations in Perovskites and Its Impact on Ion Migration

Jie Cao, Shu Xia Tao, Peter A. Bobbert, Ching-Ping Wong,* and Ni Zhao*

Recent success in achieving highly stable Rb-containing organolead halide perovskites has indicated the possibility of incorporating small monovalent cations, which cannot fit in the lead-halide cage with an appropriate tolerance factor, into the perovskite lattice while maintaining a pure stable "black" phase. In this study, through a combined experimental and theoretical investigation by density functional theory (DFT) calculations on the incorporation of extrinsic alkali cations (Rb^+, K^+, Na^+, and Li^+) in perovskite materials, the size-dependent interstitial occupancy of these cations in the perovskite lattice is unambiguously revealed. Interestingly, DFT calculations predict the increased ion migration barriers in the lattice after the interstitial occupancy. To verify this prediction, ion migration behavior is characterized through hysteresis analysis of solar cells, electrical poling, temperature-dependent conductivity, and time-dependent photoluminescence measurements. The results collectively point to the suppression of ion migration after lattice interstitial occupancy by extrinsic alkali cations. The findings of this study provide new material design principles to manipulate the structural and ionic properties of multication perovskite materials.

Organometal halide perovskite solar cells (PSCs) have attracted tremendous attention in recent years because of their rapidly rising efficiency from 3.8%[1] to over 20%[2] and the extraordinary optoelectronic properties of the perovskite active layer. The general chemical formula of perovskite materials is ABX_3, where A is a monovalent organic (methylammonium, MA^+ or formamidinium, FA^+) or inorganic (Cs^+) cation, or a mixture of both; B is Pb^{2+} or Sn^{2+}, or a mixture of both; and

X is a halide anion (I^-, Br^- or Cl^- or their mixture). Tuning the ABX_3 composition has been widely reported to not only affect the efficiency of the PSCs but also greatly impact on the stability of the perovskite layer. Accordingly, compositional effects have become a critical area for both fundamental research and device optimization.[3–8]

Among the various perovskite analogs, $MAPbI_3$ and $FAPbI_3$ are the first two material systems that have demonstrated high photovoltaic efficiency,[9–18] and have also been studied extensively in terms of stability. It was found that $FAPbI_3$ has a better thermal stability than $MAPbI_3$,[17–22] however, it lacks structural stability at room temperature because of weak interactions between the FA cation and the inorganic framework, and an undesirable yellow δ-phase is usually formed in the $FAPbI_3$ film.[19,20] Recently, the limitations of pure $MAPbI_3$ and $FAPbI_3$ systems have been addressed by using mixed A cations. Pellet et al. developed MA/FA mixed perovskites and found that the yellow δ-phase of $FAPbI_3$ could be suppressed.[3] Additionally, Lee et al. discovered that partially substituting FA^+ with Cs^+ not only induced a preferable crystallization of FA perovskite into a photoactive phase but also enhanced the moisture-stability and thermal stability of $FAPbI_3$.[4] Furthermore, McMeekin et al. observed that the phase instability issue of wide-bandgap (1.75 eV) Br–I mixed halide FA perovskites could be resolved through incorporating Cs, making it a promising perovskite absorber for tandem solar cells.[5] The improved structural stability was explained by Yi et al., elucidating that Cs assists the crystallization of the black phase in the FA perovskites due to entropic stabilization.[6] Saliba et al. developed a more complex Cs/MA/FA triple cation perovskite with improved stability, efficiency, and reproducibility of the PSCs.[7] The same researchers later reported that incorporating a small amount of Rb^+ cations in the perovskite further improved the efficiency and photostability of the Cs/MA/FA PSCs.[8] More recently, smaller alkali cations, such as K^+ and Na^+, were introduced into $MAPbI_3$ or MA/FA mixed perovskite precursor solution to tune the perovskite thin film morphology[23–25] and electronic properties.[26–30] It is argued that the incorporation of these small alkali cations can improve charge injection property or reduce trap density, thus eliminating current–voltage (I–V) hysteresis and promoting the efficiency and stability of the PSCs.[26,28] During the preparation of this manuscript, we became aware

J. Cao, Prof. C.-P. Wong, Prof. N. Zhao
Department of Electronic Engineering
The Chinese University of Hong Kong
Shatin, New Territories, Hong Kong
E-mail: cpwong@cuhk.edu.hk; nzhao@ee.cuhk.edu.hk
Dr. S. X. Tao, Prof. P. A. Bobbert
Center for Computational Energy Research
Department of Applied Physics
Eindhoven University of Technology
P. O. Box 513, 5600 MB Eindhoven, The Netherlands
Prof. P. A. Bobbert
Molecular Materials and Nanosystems
Department of Applied Physics
Eindhoven University of Technology
P. O. Box 513, 5600 MB Eindhoven, The Netherlands

The ORCID identification number(s) for the author(s) of this article can be found under https://doi.org/10.1002/adma.201707350.
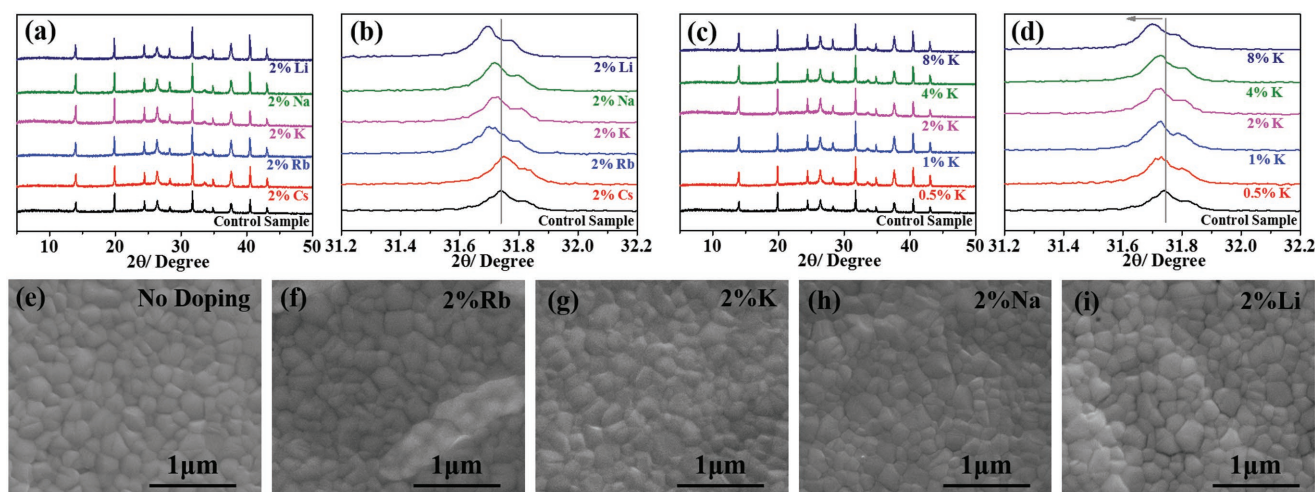
Figure 1. Phase and morphology characterizations of Cs/MA/FA perovskite with and without alkali cation doping. a) XRD patterns and (b) zoom-in to the (310) peak of the XRD patterns of 2% Cs$^+$, Rb$^+$, K$^+$, Na$^+$, or Li$^+$ embedded Cs/MA/FA perovskite. c)XRD patterns and (d) zoom-in to the (310) peak of the XRD patterns of K$^+$-doped Cs/MA/FA perovskite with various K$^+$ concentrations. SEM images of (e) Cs/MA/FA perovskite, (f) 2% Rb$^+$-doped Cs/MA/FA perovskite, (g) 2% K$^+$-doped Cs/MA/FA perovskite, (h) 2% Na$^+$-doped Cs/MA/FA perovskite, and (i) 2% Li$^+$-doped Cs/MA/FA perovskite films.

of an experimental work[31] investigating the influence of different alkali cations (Cs$^+$, Rb$^+$, K$^+$, Na$^+$, and Li$^+$) on the structural and electronic properties of MA/FA perovskite thin films, and the authors observed perovskite lattice expansion after incorporation of K$^+$, Na$^+$ or Li$^+$ and the corresponding bandgap variation. Interestingly, Rb$^+$, K$^+$ and Na$^+$ and Li$^+$ have a small ionic radius with unfavorable Goldschmidt tolerance factor for occupying the A site of the Pb–I network.[22] This observation indicates that the incorporation of extrinsic alkali cations may occur through different mechanisms, which could add another dimension for tuning the lattice structure of perovskite materials. How these extrinsic cations occupy in the perovskite lattice has not been investigated so far.

Besides thermal decomposition and lattice distortion, ion migration (resulting from the diffusion of native defects) is another thermodynamic process often associated with instability, such as photoinduced phase segregation in wide-bandgap perovskite materials[32,33] and ion migration-induced degradation of perovskites in the presence of oxygen and light.[34,35] Ion migration also accounts for anomalous device behaviors such as I–V hysteresis in PSCs[36–42] and a switchable photovoltaic effect.[43] Experimental and theoretical studies by Frost and Walsh.[38] asserted that the prevalent ion migration process in perovskites is vacancy-mediated anion (i. e., I$^-$ or Br$^-$) diffusion. The diffusion of the anions was predicted to be affected by their local chemical environment,[44–47] including the orientation of the organic cations[45] and the formation energy of the defects.[36,46,47] Experimentally, the ionic transport properties can be varied through material fabrication processes or ambient conditions, which essentially modify the composition, morphology, or defect concentration of the perovskite films. Suppressing ion migration is not a trivial task. Methods such as increasing crystal size and controlling grain boundary defects have been proposed.[13,47] Since both the presence of defects and their migration is intrinsic to perovskites,[44–49] the development of strategies to eliminate or suppress ion migration in the bulk is essential.

In this study, we explore a new mechanism to suppress ion migration in bulk perovskites through the interstitial incorporation of small alkali cations in the lattice of state-of-the-art Cs/MA/FA triple cation perovskites. First, we demonstrate that incorporating extrinsic alkali cations (i.e., Rb$^+$, K$^+$, Na$^+$, or Li$^+$) into Cs/MA/FA perovskite introduces lattice expansion, which is typically associated with interstitial occupancy of ions. Through density functional theory (DFT) calculations of the thermodynamic and kinetic properties of the possible ion incorporation patterns, we discovered that interstitial occupancy by extrinsic alkali cations is indeed energetically more favorable than A site substitution. Interestingly, the DFT calculations also predict increased ion migration barriers in the lattice after the interstitial occupancy. To verify this theoretical prediction, we characterized the ion migration behavior via hysteresis analysis of solar cells, electrical poling, temperature-dependent conductivity, and time-dependent photoluminescence (PL) measurements. The results collectively point to the suppression of ion migration after the lattice interstitial occupancy by extrinsic alkali cations.

Thin films of Cs$_{0.11}$MA$_{0.15}$FA$_{0.74}$Pb(Br$_{0.17}$I$_{0.83}$)$_3$ (abbreviated as Cs/MA/FA for convenience) perovskite were used as the control sample and fabricated by depositing the precursor solution on a SnO$_2$-coated fluorine doped tin oxide (FTO) substrate according to a previously reported spin-coating process[50] (described in detail in the Experimental section). To introduce the extrinsic alkali cations (Rb$^+$, K$^+$, Na$^+$, or Li$^+$) into the perovskite films, their corresponding iodide salt (RbI, KI, NaI, or LiI) was added to the Cs/MA/FA perovskite precursor solution with varying molar concentrations from 0.5 to 8%. The percentage was referred as the molar concentration of the alkali cations in the perovskite precursor solution. After formation of the perovskite films, we first investigated the effect of the extrinsic alkali cations on the perovskite crystal structure and film morphology. The X-ray diffraction (XRD) patterns in **Figure 1**a and the scanning electron microscopy (SEM) images in Figure 1e–i collectively demonstrate that incorporating 2% extrinsic alkali
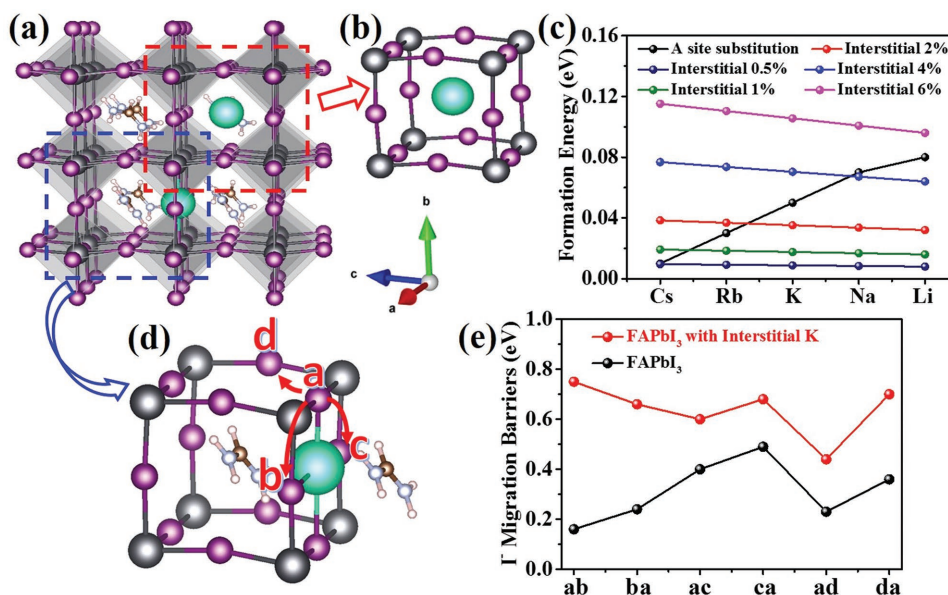
Figure 2. Thermodynamic and kinetic properties of alkali cation incorporation (Cs^+, Rb^+, K^+, Na^+, and Li^+). a) Illustration of the possible locations of alkali cations in $FAPbI_3$: b) at the A site and (d) at the interstitial site. c) ΔH_{0K} of alkali cation incorporation at an A site (being constant for concentration from 0.5 to 6%) and at an interstitial site. Values are estimated based on Table S2 and Figure S3 (Supporting Information). d) Illustration of the I^- diffusion pathways, using $FAPbI_3$ perovskite with K^+ at an interstitial site as an example. e) Comparison of the I^- diffusion barriers in $FAPbI_3$ with and without interstitial K^+. The lines are guides to the eye.

cations does not change the crystallinity or morphology of the Cs/MA/FA perovskite films. However, when zooming in to the main peak corresponding to the (310) crystal planes of the perovskite (Figure 1b), a clear peak shift toward lower angles is observed. Generally, substitution of perovskite A cations (i.e., FA^+, MA^+, or Cs^+) with smaller cations results in lattice contraction, and thus a shift of the main XRD peak to a higher angle.[3–5] Indeed, when we added an additional 2% Cs^+ to the Cs/MA/FA perovskite, we observed a slight shift of the XRD peak toward a higher angle, corresponding to a lattice contraction due to the smaller size of Cs^+ as compared to FA^+ and MA^+ (Figure S1a,b, Supporting Information). Therefore, the opposite shift of the XRD peak to a lower angle may correspond to lattice expansion, which could occur through interstitial occupancy by the alkali cations or the reduction of bromide anion in the lattice. In order to determine which of the above is the dominant mechanism, we further incorporated RbI, KI, NaI or LiI into the pure iodide precursors of $Cs_{0.11}MA_{0.15}FA_{0.74}PbI_3$. As shown in Figure S2 (Supporting Information), for the pure iodide perovskites, the main XRD peaks also shifted to a lower angle, suggesting that the perovskite lattice expansion should mainly result from the interstitial occupancy of alkali cations. The theoretical validation of such interstitial occupancy will be described in the next section. We also noted that no new phase was formed in the K^+- or Na^+-doped perovskites when the doping concentration was increased from 0.5 to 8% (Figure 1c; Figure S1e, Supporting Information), whereas >2% Rb^+ or Li^+ doping readily resulted in precipitation of a secondary phase δ-$RbPbI_3$[8,51–53] (Figure 1f; Figure S1c, Supporting Information) or δ-$CsPbI_3$ (Figure S1g, Supporting Information) phases in the perovskites, manifesting a size-dependent dopant concentration tolerance.

To verify the hypothesis of alkali ion occupancy at the interstitial site of the perovskite lattice, we subsequently investigated the energetics and the alkali cation incorporation mechanisms by using DFT calculations. We calculated and compared the formation energies (ΔH_{0K}) at zero temperature (0 K) of the pure $FAPbI_3$ perovskite and $FAPbI_3$ with alkali cations (Cs^+, Rb^+, K^+, Na^+, and Li^+) incorporated at an A site or interstitial site (i.e., the site between two A sites, as shown in **Figure 2**b,d). Detailed descriptions of the reactions, the model choices, and the methodology can be found in the Computational Methods section. The results of thermodynamics of the pure perovskites without alkali cations are also provided in Table S1 (Supporting Information).

We investigated alkali cation substitution at an A site or occupancy at an interstitial site in $FAPbI_3$, $MAPbI_3$, $FAPbBr_3$, $MAPbBr_3$ perovskite lattices. Because FA^+ as a cation and I^- as an anion are the most abundant species in the experimentally studied $FA_xMA_{1-x}Pb(I_yBr_{1-y})_3$ system, the ΔH_{0K} of alkali cation (Cs^+, Rb^+, K^+, Na^+, and Li^+) incorporation with several concentrations in $FAPbI_3$ (Figure 2c; Table S2 and Figure S3, Supporting Information) perovskites are mainly analyzed (results for other material systems are also provided in Figure S4 in the Supporting Information). In general, we observe that incorporating alkali cations at either an A site or an interstitial site yields a more positive ΔH_{0K} than the pure perovskite host because of lattice volume shrinkage (in the case of A site substitution) or lattice volume expansion (in the case of interstitial site occupancy). Specifically, the variation of ΔH_{0K} exhibits the following trends (Figure 2c):

1) The ΔH_{0K} of the interstitial occupancy increases linearly with increasing alkali cation concentration. In contrast, the change in ΔH_{0K} for A-site substitution as a function of alkali
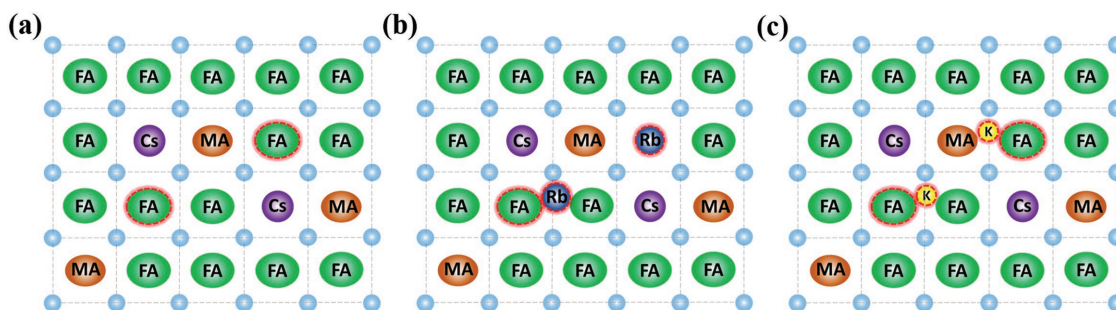
ADVANCED
SCIENCE NEWS
www.advancedsciencenews.com

ADVANCED
MATERIALS
www.advmat.de

Figure 3. Schematics of the doping mechanism of Cs/MA/FA perovskite doped with Cs^+, Rb^+, and K^+. a) Side view of the original Cs/MA/FA perovskite lattice structure. b) Side view of the lattice structure of Cs/MA/FA perovskite doped with Rb^+. c) Side view of the lattice structure of Cs/MA/FA perovskite doped with K^+.

cation concentration is minor and almost reaches zero for low alkali cation concentrations (<12.5%).

2) The increase in ΔH_{0K} is cation size-dependent: a) For A site substitution, the larger the alkali ions, the smaller the increase in ΔH_{0K}; the difference in ΔH_{0K} between the largest (Cs^+) and smallest (Li^+) ion substitution is large (i.e., 0.07 eV). b) For interstitial occupancy, the opposite holds; the difference in ΔH_{0K} between the interstitial occupancy of the largest (Cs^+) and smallest (Li^+) cations is small (i.e., 0.01–0.02 eV).

The combination of these trends leads to the following conclusions: 1) Both types of occupancy are thermodynamically possible when the percentage of alkali cations is small (≤6%). 2) When the concentration of alkali cations decreases, the interstitial occupancy starts to be favorable; and the smaller the alkali cation, the higher the concentration below which it tends to prefer the interstitial sites. 3) Even at very low concentration (0.5%), the interstitial occupancy of the largest alkali cations (Cs^+) is still less favorable than A site occupancy. In addition, we also explored the possibility of incorporating alkali cations (Cs^+, Rb^+, K^+, Na^+, and Li^+) at the B site (Pb) of $FAPbI_3$ perovskite. As Table S3 (Supporting Information) shows, the formation energies of B site substitution are significantly higher than both A site substitution and interstitial site occupancy for all alkali cations regardless of their ionic radius (Cs^+, Rb^+, K^+ are larger and Na^+ and Li^+ are smaller than Pb^{2+}). Further evidence for the favorable energetics of interstitial occupancy for extrinsic alkali cations is provided by analysis of the diffusion barrier of the alkali cations reported in Figure S5 (Supporting Information).

To illustrate the theoretical findings, we propose a lattice model schematically depicted in **Figure 3**. Figure 3a–c shows a side view of the lattice structure of the Cs/MA/FA perovskite lattice without (a) and with small amounts of Rb^+ (b) and K^+ (c) incorporated in the lattice. Being a large cation, Cs^+ is demonstrated both experimentally (our work and previous works[3–5]) and theoretically to occupy the A sites. Rb^+ has an intermediate size. Therefore, Rb^+ can be incorporated at both types of sites and can easily diffuse between these types of sites (Figure S5, Supporting Information). Finally, the small K^+ tends to occupy the interstitial sites, evidenced by the favorable thermodynamics and sizable diffusion barriers to the A sites (Figure S5, Supporting Information).

We further extended the theoretical investigation to the question how the interstitial ions affect the migration of ionic native defects (i. e., iodide or bromine vacancy), a prevailing process in organolead halide perovskites that is often associated with $I–V$ hysteresis in PSCs[39–42,44–48] and photoinduced phase separation.[32,33] We calculated vacancy-mediated I^- diffusion with and without alkali cation K^+ interstitial occupancy in $FAPbI_3$. As shown in Figure 2d, we investigated several diffusion pathways (ab, ac, and ad) to distinguish the influence of the local environment on individual diffusion paths. The environmental effect of each path can be identified based on the distance to the interstitial alkali cations (ab vs ad), the orientation of the FA cations (ab vs ac), or the direction of the diffusion paths (ab vs ba). The calculated I^- diffusion barriers are found to range from 0.16 to 0.49 eV. This energy range is comparable to several DFT results for $FAPbI_3$,[47,54] $MAPbI_3$, which range from 0.08 to 0.65 eV using different approximation schemes, different DFT codes, and taking into account several local environments.[36,42,44–47]

As shown in Figure 2e, the incorporation of interstitial K^+ leads to sizable increase in the diffusion barriers for all diffusion paths (from 0.11 to 0.59 eV). Through careful analysis of the trends in the diffusion barriers and their associated atomic arrangement, we determined three main roles of the interstitial K^+ in increasing diffusion barriers. First, the K^+ suppresses the I^- diffusion through partially blocking of the diffusion pathways. Second, more energy is required to create an iodide vacancy when K^+ cations are present than when they are not, as evidenced by the increased formation energies in Table S4 (Supporting Information). Third, the incorporation of K^+ cations alters the orientation of the FA^+ cations, by pulling these cations from their original (111) orientation to (110) orientation (Figure S6, Supporting Information), in order to maximize their interaction with the surrounding FA cations. The result of this reorientation is also a change of the dipole direction, pointing more in the direction of the K^+, and consequently alters the I^- diffusion barriers. The dipole-orientation-induced diffusion barriers were also found in $MAPbI_3$,[45] although with a much larger range of the activation barriers (0.06 to 0.65 eV). This large range of activation barriers is probably due to the larger dipole moment of the MA cation as compared to the FA cation.[38]

The DFT calculation results predict increased ion migration barriers through K^+ interstitial occupancy. To verify this prediction, we characterized the ion migration behavior through $I–V$ hysteresis analysis of the PSCs, electrical poling,
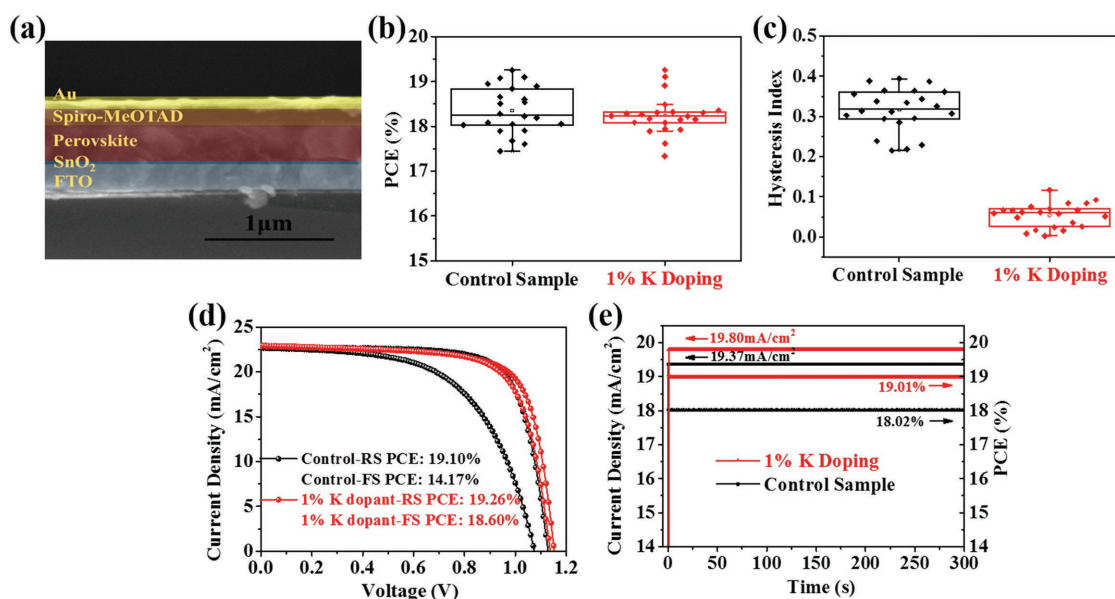
Figure 4. Impact of interstitial doping on PSC performance. a) Cross-sectional SEM image of the PSC structure. b) Comparison of the PCE (extracted from the reverse scans of the J–V curves) of the PSCs without doping and with 1% K^+ doping. c) Comparison of the hysteresis index of the PSCs without doping and with 1% K^+ doping. The statistics of the PCE and hysteresis index in panels (b) and (c) are based on 22 devices for each condition. The tiny box within the large box indicates mean value. The upper and lower bars represent standard deviation from the mean value, and the middle line in each box represents the median value. Upper and lower borderlines of the box represent the third quartile (Q3) and first quartile (Q1), respectively, and the box thickness represents interquartile range Q3–Q1. d) J–V curves from the reverse and forward scans of the PSCs without doping and with 1% K^+ doping. e) Steady-state current density and PCE of the PSCs without doping and with 1% K^+ doping (the device without doping was biased at 0.93 V and the device with 1% K^+ doping was biased at 0.96 V).

temperature-dependent conductivity, and time-dependent PL measurements of the perovskite materials.

We first studied the I–V hysteresis of the PSCs based on the Cs/MA/FA perovskite films. The perovskite films with various alkali cation species and doping concentrations were incorporated into the device with the structure FTO/SnO$_2$/perovskite/N2,N2,N2′,N2′,N7,N7,N7′,N7′-octakis(4-methoxyphenyl)-9,9′-spirobi[9H-fluorene]-2,2′,7,7′-tetramine (spiro-MeOTAD)/Au (**Figure** 4a). The current density–voltage (J–V) curves of the corresponding PSCs are presented in Figure S7 (Supporting Information). We extracted the power conversion efficiency (PCE, from the reverse scan) and the hysteresis index, HI[53]

$$\left(HI = \frac{PCE_{reverse} - PCE_{forward}}{PCE_{reverse}} \right),$$

from the J–V curves (Figure S7, Supporting Information) and summarized them in Table S5 (Supporting Information) to analyze the variation of the PCE and J–V hysteresis as a function of doping concentration. We also noted that the J–V hysteresis of the PSCs is highly related to the preconditioning treatment of the devices, such as exposure to the applied bias, light illumination or dark, and varied scan rates.[41,55–57] In order to fairly compare the hysteresis behavior of the PSCs with and without doping, we adopted the commonly used J–V measurement for all the devices without any intended preconditioning treatment, i.e., no bias, no preillumination and with a scan rate of 0.1 V s^{-1}. We analyzed the variation of the PCE and J–V hysteresis as a function of doping concentration. We found that additional Cs$^+$ or Li$^+$ incorporation had no positive effect on the hysteresis of the Cs/MA/FA PSCs; by contrast, Rb$^+$, K$^+$, and Na$^+$ doping at appropriate

concentrations dramatically reduced hysteresis. This result agrees well with the DFT prediction of suppressed I$^-$ migration, whereas the large hysteresis observed in Li$^+$-doped PSCs could be attributed to the small size and high mobility of Li$^+$ cations,[58] which were not considered in the DFT calculations. It was also noted that increasing the Rb$^+$ concentration to over 2% in the perovskite deteriorated the device performance, whereas increasing the Li$^+$ or Na$^+$ concentration to over 4% adversely increased the hysteresis. The decreased PCE of the PSCs with a high Rb concentration resulted from the formation of photoinactive δ-RbPbI$_3$ impurities in the perovskite film, and the increased hysteresis of the PSCs with a high Na$^+$ concentration resulted from additional Na$^+$ migration in the perovskites.[58]

By comparing all PSC devices, we conclude that K$^+$ incorporation yields the widest doping concentration window for effectively reducing hysteresis while maintaining high photovoltaic efficiency, coinciding with the results of a very recent work reporting that incorporating K into the Cs/MA/FA perovskite reduced the hysteresis of PSCs.[59] Figure 4b–e displays the PCE statistics, HI statistics, J–V curves, and stabilized power output of the PSCs with 1% K$^+$ doping and without doping, respectively. The PSCs with 1% K$^+$ doping demonstrated improved stabilized PCE from 18 to 19% (Figure 4e), which, according to Figure 4c, is associated with reduced hysteresis. We also embedded K$^+$ into MA/FA perovskites, and again observed the lattice expansion and reduced hysteresis of PSCs, as shown in Figure S8 and Table S6 in the Supporting Information, demonstrating the universality of interstitial doping in the mixed-cation perovskite materials. We note that the I–V hysteresis is a combination effect of ion migration and charge trapping (or

ADVANCED
SCIENCE NEWS
www.advancedsciencenews.com
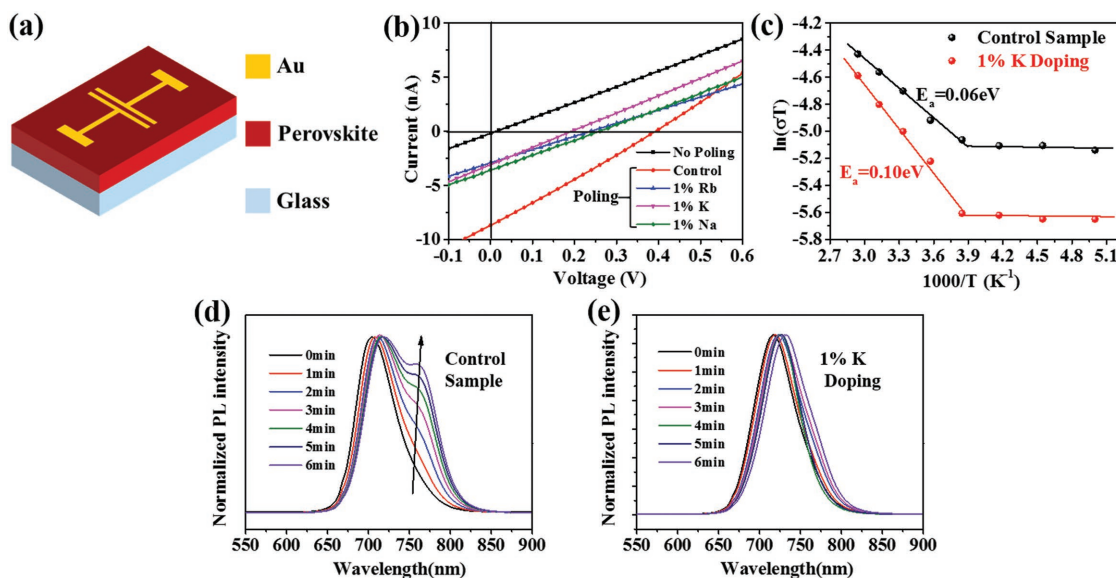
ADVANCED
MATERIALS
www.advmat.de

Figure 5. Optical and electrical characterizations of the ion migration behaviors of the perovskite films. a) Device structure for electrical poling of the perovskite films. b) I–V curves of the devices with various dopants before and after poling at 1 V μm^{-1} for 30 s. c) Extraction of the activation energy from the temperature-dependent conductivity measurement of Cs/MA/FA perovskite and 1% K$^+$-doped Cs/MA/FA perovskite. Normalized PL spectra measured after 0–6 min of light exposure of the (d) $Cs_{0.11}MA_{0.15}FA_{0.74}PbBr_{1.2}I_{1.8}$ and (e) 1% K$^+$-doped $Cs_{0.11}MA_{0.15}FA_{0.74}PbBr_{1.2}I_{1.8}$ thin films.

trapping induced charge recombination);[40,41,60] thus, the hysteresis phenomenon could be alleviated by either suppressing ion migration or reducing charge trapping at the perovskite/charge transport layer interface. In our experiment, the alkali cations were incorporated into the perovskite film through modification of precursor solution, and we have confirmed with X-ray photoelectron spectroscopy depth profiling that the alkali cations distribute uniformly throughout the perovskite film (data not shown); therefore, the interface passivation effect by the alkali cations is quite unlikely, and the observed hysteresis reduction should originate from suppressed ion migration.

To confirm that the reduced hysteresis was not caused by an interface modification effect in the PSCs, we examined the ion migration behavior through electrical poling[43,61] experiments in a lateral conductor device structure (**Figure 5**a). In such experiments, a constant bias is applied between two parallel electrodes with 100 μm spacing, generating an electric field that induces a drift of the charged ions or defects. Accordingly, regions with p-type doping by negatively charged ions/vacancies and n-type doping by positively charged ions/vacancies are created next to the positive and negative electrodes, respectively,[62–64] resulting in a reversible p–i–n structure in the perovskite layer.[43] Upon illumination, the poled device generates an open-circuit voltage (V$_{oc}$), the magnitude of which is determined by the built-in potential (V$_{bi}$) of the p–i–n structure. V$_{oc}$ is essentially determined by the doping concentration on the p and n sides. Specifically, the more ions piled up at the electrodes, the higher the V$_{oc}$. As shown in Figure 5b, the nonpoled triple cation (Cs/MA/FA) perovskite device yielded zero V$_{oc}$ because of the symmetry of the electrode structure; after poling the device at 100 V for 30 s, a photovoltaic effect under 1 sun illumination was observed, with a V$_{oc}$ of 0.38 V. By contrast, the perovskite with 1% K$^+$ doping exhibited a nearly halved V$_{oc}$ of 0.2 V after the same poling process, clearly indicating reduced

ion migration. Similar results were obtained for perovskite devices with Rb$^+$ or Na$^+$ doping (Figure 5b) and with various poling electric fields (Figure S9, Supporting Information).

Using the conductor structure, we further characterized the activation energy (E$_a$) of ion migration in the pure and K$^+$-doped Cs/MA/FA perovskite materials through temperature-dependent conductivity measurement. The conductivity values under various temperatures were extracted from the J–V curves under dark condition, which were then used to calculate activation energy through Nernst–Einstein relation[65]: $\sigma(T) = (\sigma_0/T) \exp(-E_a/kT)$, where k is Boltzmann's constant, σ_0 is a constant, and T is the temperature. As shown in Figure 5c, two slopes are identified from each dataset, likely corresponding to two conduction mechanisms: electronic conduction and ionic conduction. In the low-temperature region (200–260 K), the ion motion is frozen or largely suppressed and the conductivity is determined by electronic conduction; when the temperature exceeds 260 K, ionic conduction begins to contribute to the electric current. The transition temperature from electronic to ionic conduction identified here is also in good agreement with the results of a recent work.[65] The conductivity increase with increasing temperature reflects the role of thermal activation in ion migration. The E$_a$ of the ionic conduction was fitted to be 0.06 and 0.10 eV for the pure and K$^+$-doped Cs/MA/FA perovskite, respectively, indicating the increased E$_a$ of the perovskite material by K$^+$ doping, which agrees well with the increased ion migration barriers predicted by the DFT calculations in Figure 2e.

Photoinduced phase segregation has been a key issue limiting the V$_{oc}$ of wide-bandgap perovskite solar cells. The process is believed to occur through ion migration. Therefore, we extended the interstitial doping treatment to wide-bandgap perovskite materials in which I$^-$ is partially replaced by Br$^-$. The Br$^-$ to I$^-$ ratio was increased from 1:5 to 2:3 while maintaining the same composition of A-site cations in the

perovskite precursor solution. The Tauc plot in Figure S10 (Supporting Information) suggests that the bandgap of the $Cs_{0.11}MA_{0.15}FA_{0.74}PbBr_{1.2}I_{1.8}$ film is 1.78 eV. We performed time-dependent PL measurements on $Cs_{0.11}MA_{0.15}FA_{0.74}PbBr_{1.2}I_{1.8}$ and 1% K^+-doped $Cs_{0.11}MA_{0.15}FA_{0.74}PbBr_{1.2}I_{1.8}$ thin films by using an excitation source with a power density of 38 mW cm^{-2} and a wavelength of 405 nm. The perovskite film without doping exhibited a rapidly rising PL peak that is red-shifted from the original one, which is a typical indication of phase segregation. By contrast, the K^+-doped perovskite film revealed highly suppressed phase segregation, as shown in Figure 5d,e. We also considered doping with other extrinsic alkali cations (Figure S11, Supporting Information). We found that Rb^+- and Na^+-doped perovskites exhibited suppressed PL peak red-shifts, whereas the Li^+-incorporated perovskite exhibited a strong time-dependent red-shift of the PL peak, which may again be related to the high mobility of Li^+ in the perovskite. The interstitial cation-enhanced photostability of wide-bandgap perovskites may be particularly useful for achieving high-efficiency tandem solar cells.

Although this study has mainly focused on K^+-doped FA/MA/Cs perovskite films, we also verified 1) the interstitial occupancy of Rb^+, Na^+, and Li^+ and 2) the ion migration suppression effects of Rb^+ and Na^+. A key difference among these alkali cations is the size-dependent doping concentration effect. The related major observations are summarized as follows. First, the large alkali cation Cs^+ prefers to occupy the A sites of the perovskite lattice, and incorporation of a small amount of excess Cs^+ in Cs/MA/FA perovskite has negligible effects on the lattice structure and hysteresis of the PSCs. Second, doping with extrinsic alkali cations of a moderate size, such as Rb^+, K^+, or Na^+, remarkably reduces the hysteresis of the PSCs. Of those cations, the large Rb^+ cations have a stronger tendency to segregate from the Pb–I cages to form a yellow phase; therefore, they can only be used at very low concentrations. The small Na^+ cations can be incorporated into the perovskite lattice at higher concentrations, but are less effective in blocking ion migration than Rb^+ and K^+ cations. Third, Li^+ cations may participate in, instead of suppress, ion migration due to their small size and high mobility, even though these cations can still occupy interstitial sites.

Taking together, the following principles should be considered when applying interstitial cations to modulate ion migration in perovskite materials. First, the "optimal size" of the interstitial cation is defined by the basic framework of the perovskite lattice (or more specifically, the size of the interstitial sites). In this study we identified K^+ as the optimal interstitial cation for $FAPbI_3$, but the conclusion may vary in other perovskite systems with significantly different lattice constant. Second, the size variation of interstitial cation always induces combined effects: on one hand, increasing the cation size will result in a higher energy barrier for ion migration; on the other hand, it will narrow down the concentration window where interstitial occupancy is energetically favored over A site occupancy. From fabrication point of view, the latter effect may not be ideal for achieving high reproducibility.

In conclusion, we successfully incorporated extrinsic alkali cations (Rb^+, K^+, Na^+, and Li^+) into Cs/MA/FA perovskite films, and experimentally as well as theoretically, based on DFT calculations, demonstrated that these alkali cations can occupy the interstitial sites of the perovskite lattice. The DFT calculations further reveal that the occupancy selection between the A site and interstitial site is cation size dependent. The DFT calculations also predict that the interstitial ions raise the migration energy barrier for native halide defects. We experimentally verified this prediction through characterizing the defect migration-related material or device behaviors upon light or electrical excitation. Our experiments indicate that the incorporation of properly sized alkali cations, such as K^+, results in reduced I–V hysteresis of PSCs, weakened poling effects, and improved photostability of wide-bandgap mixed-halide perovskites, all pointing to suppressed ion migration. This study not only highlights the possibility of the incorporation of interstitial cations in the perovskite lattice but also suggests a simple bottom-up approach to manipulate the local structural and ionic properties of perovskite films without altering the film morphology and crystallinity.

Experimental Section

Perovskite Precursor Solution: MA/FA perovskite: 1.1 M PbI$_2$ (Sigma-Aldrich), 0.22 M PbBr$_2$ (Sigma-Aldrich), 1 M FAI (Dyesol), and 0.2 M MABr (Dyesol) were dissolved in a mixture of anhydrous DMF/DMSO with a volume ratio of 4:1.

MA/FA/Cs perovskite: 1.5 M stock solution of CsI in DMSO was added to a MA/FA mixed perovskite solution with a volume ratio of 10:90.

MA/FA/K perovskite: Different amounts of 1.5 M stock solution of KI in DMSO/DMF (a volume ratio of 1:4) were added to a MA/FA mixed perovskite solution.

MA/FA/Cs/Rb, MA/FA/Cs/K, MA/FA/Cs/Na or MA/FA/Cs/Li perovskite: Different amounts of 1.5 M stock solution of RbI, KI, NaI or LiI in DMSO/DMF (a volume ratio of 1:4) were added to a MA/FA/Cs mixed perovskite solution. Because NaI and LiI are badly solvable in DMF or DMSO, the NaI and LiI solutions were kept under 70 °C when preparing the Na or Li doped MA/FA/Cs perovskite precursor solution.
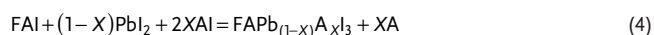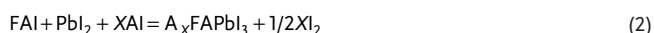
MA/FA/Cs perovskite with wide bandgap: 0.77 M PbI$_2$, 0.55 M PbBr$_2$, 0.7 M FAI, and 0.5 M MABr were dissolved in a mixture of anhydrous DMF/DMSO with a volume ratio of 4:1. 1.5 M stock solution of CsI in DMSO was successively added to the MA/FA mixed perovskite solution with a volume ratio of 10:90.

Solar Cell Fabrication: FTO (DHS-FTO22-15N, HeptaChroma) substrates were subsequently cleaned with detergent, deionized water, acetone, and 2-propanol, followed by an UV–ozone (PSD-UV8, NOVASCAN) treatment for 15 min. The SnO$_2$ electron transport layer was spin-coated onto the FTO substrate by a modified process reported in the previous work.[66] The spin-coating rate was set at 3000 rpm for 30 s, followed by a gradient heating and baking at 180 °C for 1 h on a hotplate. After cooling to room temperature, all SnO$_2$ layers were treated by an UV–ozone machine for 15 min. Then, all SnO$_2$ coated FTO substrates were transferred to the glove box for the fabrication of the perovskite layer and spiro-MeOTAD hole transport layer. All perovskite layers were deposited through a consecutive two-step spin-coating process (1000 rpm for 5 s and 6000 rpm for 30 s), and 12 s before the end of the second step, 160 µL chlorobenzene as antisolvent was dripped on the perovskite, followed by annealing at 100 °C for 1 h. The N2,N2,N2′,N2′,N7,N7,N7′,N7′-octakis(4-methoxyphenyl)-9,9′-spirobi[9H-fluorene]-2,2′,7,7′-tetramine (spiro-MeOTAD) hole transport layer was prepared by spin-coating a precursor solution consisting of 72.3 mg spiro-MeOTAD, 28.8 µL 4-tert-butylpyridine and 17.5 µL lithium-bis(trifluoromethanesulfonyl)imide (Li-TFSI) solution (520 mg Li-TFSI in 1 mL acetonitrile) in 1 mL chlorobenzene onto the perovskite layer at 4000 rpm for 30 s. Finally, a 80 nm thick gold electrode was deposited via thermal evaporation with a mask area of 0.05 cm^2.

Measurement and Characterization: The crystal phases of the perovskite films were identified by an X-ray diffraction system with a Rigaku ru-300 diffractometer using $CuK\alpha_1$ irradiation ($\lambda = 1.5406$ Å). Pictures of the film morphologies and the cross-section of the device structure were made by high-resolution field emission scanning electron microscopy (HR-FESEM, FEI, Quanta 400). The current–voltage (*I–V*) curves were measured with a scan rate of 0.1 V s^{-1} (Keithley Instruments, 2612 Series SourceMeter) under simulated AM 1.5 sunlight (100 mW cm^{-2}) generated by a 94011A-ES Sol series Solar Simulator. PL measurements were taken by a continuous-wave laser source with a wavelength of 405 nm and a power density of 38 mW cm^{-2} at room temperature. The electrical poling of the device was conducted by applying different biases on the electrodes with 100 µm spacing for 30 s in the dark, and the current–voltage (*I–V*) curves were measured under simulated AM 1.5 sunlight (100 mW cm^{-2}) by a Keithley 2612 source meter.

Computational Methods: DFT calculations were performed at the level of GGA in the Perdew–Burke–Ernzerhof (PBE)[67] parameterization as implemented in the Vienna ab initio simulation package (VASP).[68–70] For hybrid halide perovskites containing MA and FA, long-range van der Waals interactions have been taken into account via the TS (Tkatchenko and Scheffler) scheme.[68] The predicted trends for the formation energies of all hybrid perovskites (MA/FAPbI/Br) using the PBE parameterization with and without van der Waals corrections are the same (see Table S1, Supporting Information). However, like most of the dispersion correction schemes, the TS correction scheme performs differently for all inorganic and hybrid systems.[71] Therefore, for the sake of consistency, the PBE parameterization without van der Waals correction was adopted when investigating the thermodynamics of the alkali ion incorporation in FA perovskites. The outermost s, p, and d (in the case of Pb) electrons are treated as valence electrons of which the interactions with the remaining ions is modeled by pseudopotentials generated within the projector-augmented wave method.[72] The diffusion barriers were calculated using the nudged elastic band method in conjunction with the climbing image method.[73–75] Unless specified otherwise, $2 \times 2 \times 2$ supercells of pseudocubic structures were modeled and allowed to fully relax (cell shape, volume, and ion positions) during the structural optimization. An energy cutoff of 500 eV and $3 \times 3 \times 3$ k-point meshes are used to achieve energy and force convergence of 0.1 meV and 2 meV Å^{-1}, respectively.

The formation of pure $FAPbI_3$ and $FAPbI_3$ with alkali metal incorporated in A, B, and interstitial sites can be described by the following reactions, respectively

$$FAI + PbI_2 = FAPbI_3 \tag{1}$$

$$FAI + PbI_2 + XAI = A_X FAPbI_3 + 1/2XI_2 \tag{2}$$

$$FAI + PbI_2 + XAI = A_X FA_{1-X} PbI_3 \tag{3}$$

$$FAI + (1-X)PbI_2 + 2XAI = FAPb_{(1-X)} A_X I_3 + XA \tag{4}$$

where X is the concentration of the A (alkali) ions incorporated in the perovskite lattice. A positive value of ΔH_{0K} indicates that the formation of the compound is thermodynamically not favorable.

Supporting Information

Supporting Information is available from the Wiley Online Library or from the author.

Acknowledgements

Conflict of Interest

The authors declare no conflict of interest.

Keywords

[1] A. Kojima, K. Teshima, Y. Shirai, T. Miyasaka, *J. Am. Chem. Soc.* **2009**, *131*, 6050.

[2] KRICT, www.nrel.gov/pv/assets/images/efficiency-chart.png (accessed: December 2017).

[3] N. Pellet, P. Gao, G. Gregori, T.-Y. Yang, M. K. Nazeeruddin, J. Maier, M. Gratzel, *Angew. Chem., Int. Ed.* **2014**, *53*, 3151.

[4] J.-W. Lee, D.-H. Kim, H.-S. Kim, S.-W. Seo, S. M. Cho, N.-G. Park, *Adv. Energy Mater.* **2015**, *5*, 1501310.

[5] D. P. McMeekin, G. Sadoughi, W. Rehman, G. E. Eperon, M. Saliba, M. T. Hörantner, A. Haghighirad, N. Sakai, L. Korte, B. Rech, M. B. Johnston, L. M. Herz, H. J. Snaith, *Science* **2016**, *351*, 151.

[6] C. Yi, J. Luo, S. Meloni, A. Boziki, N. A. Astani, C. Grätzel, S. M. Zakeeruddin, U. Röthlisberger, M. Grätzel, *Energy Environ. Sci.* **2016**, *9*, 656.

[7] M. Saliba, T. Matsui, J.-Y. Seo, K. Domanski, J.-P. Correa-Baena, M. K. Nazeeruddin, S. M. Zakeeruddin, W. Tress, A. Abate, A. Hagfeldt, M. Grätzel, *Energy Environ. Sci.* **2016**, *9*, 1989.

[8] M. Saliba, T. Matsui, K. Domanski, J.-Y. Seo, A. Ummadisingu, S. M. Zakeeruddin, J.-P. Correa-Baena, W. R. Tress, A. Abate, A. Hagfeldt, M. Grätzel, *Science* **2016**, *354*, 206.

[9] M. M. Lee, J. Teuscher, T. Miyasaka, T. N. Murakami, H. J. Snaith, *Science* **2012**, *338*, 643.

[10] M. Liu, M. B. Johnston, H. J. Snaith, *Nature* **2013**, *501*, 395.

[11] Q. Chen, H. Zhou, Z. Hong, S. Luo, H. S. Duan, H. H. Wang, Y. Liu, G. Li, Y. Yang, *J. Am. Chem. Soc.* **2014**, *136*, 622.

[12] J. Burschka, N. Pellet, S. J. Moon, R. Humphry-Baker, P. Gao, M. K. Nazeeruddin, M. Grätzel, *Nature* **2013**, *499*, 316.

[13] Y. Shao, Z. Xiao, C. Bi, Y. Yuan, J. Huang, *Nat. Commun.* **2014**, *5*, 5784.

[14] G. Xing, N. Mathews, S. Sun, S. S. Lim, Y. M. Lam, M. Grätzel, S. Mhaisalkar, T. C. Sum, *Science* **2013**, *342*, 344.

[15] Q. Dong, Y. Fang, Y. Shao, P. Mulligan, J. Qiu, L. Cao, J. Huang, *Science* **2015**, *347*, 967.

[16] J. Cao, F. Wang, H. Yu, Y. Zhou, H. Lu, N. Zhao, C.-P. Wong, *J. Mater. Chem. A* **2016**, *4*, 10223.

[17] X. Zhao, N.-G. Park, *Photonics* **2015**, *2*, 1139.

[18] Y.-Y. Zhang, S. Chen, P. Xu, H. Xiang, X.-G. Gong, A. Walsh, S.-H. Wei, *Chin. Phys. Lett.* **2018**, *35*, 036104.

[19] S. Pang, H. Hu, J. Zhang, S. Lv, Y. Yu, F. Wei, T. Qin, H. Xu, Z. Liu, G. Cui, *Chem. Mater.* **2014**, *26*, 1485.

[20] J.-W. Lee, D.-J. Seol, A.-N. Cho, N.-G. Park, *Adv. Mater.* **2014**, *26*, 4991.

[21] F. Wang, H. Yu, H. Xu, N. Zhao, *Adv. Funct. Mater.* **2015**, *25*, 1120.

[22] Q. Han, S.-H. Bae, P. Sun, Y.-T. Hsieh, Y. (Michael) Yang, Y. S. Rim, H. Zhao, Q. Chen, W. Shi, G. Li, Y. Yang, *Adv. Mater.* **2016**, *28*, 2253.

[23] M. M. uz Zaman, M. Imran, A. Saleem, A. H. Kamboh, M. Arshad, N. A. Khan, P. Akhter, *Phys. B: Condens. Matter* **2017**, *522*, 57.

[24] K. M. Boopathi, R. Mohan, T.-Y. Huang, W. Budiawan, M.-Y. Lin, C.-H. Lee, K.-C. Ho, C.-W. Chu, *J. Mater. Chem. A* **2016**, *4*, 1591.

[25] M. Abdi-Jalebi, M. I. Dar, A. Sadhanala, S. P. Senanayak, M. Franckevi̇us, N. Arora, Y. Hu, M. K. Nazeeruddin, S. M. Zakeeruddin, M. Grätzel, R. H. Friend, *Adv. Energy Mater.* **2016**, *6*, 1502472.

[26] Z. Tang, T. Bessho, F. Awai, T. Kinoshita, M. M. Maitani, R. Jono, T. N. Murakami, H. Wang, T. Kubo, S. Uchida, H. Segawa, *Sci. Rep.* **2017**, *7*, 12183.

[27] J. K. Nam, S. U. Chai, W. Cha, Y. J. Choi, W. Kim, M. S. Jung, J. Kwon, D. Kim, J. H. Park, *Nano Lett.* **2017**, *17*, 2028.

[28] P. Zhao, W. Yin, M. Kim, M. Han, Y. J. Song, T. K. Ahn, H. S. Jung, *J. Mater. Chem. A* **2017**, *5*, 7905.

[29] M. Abdi-Jalebi, Z. A. -Garmaroudi, S. Cacovich, C. Stavrakas, B. Philippe, J. M. Richter, M. Alsari, E. P. Booker, E. M. Hutter, A. J. Pearson, S. Lilliu, T. J. Savenije, H. Rensmo, G. Divitini, C. Ducati, R. H. Friend, S. D. Stranks, *Nature* **2018**, *555*, 497.

[30] W. Zhao, Z. Yao, F. Yu, D. Yang, S. (Frank) Liu, *Adv. Sci.* **2018**, *5*, 1700131.

[31] Z. Tang, S. Uchida, T. Bessho, T. Kinoshita, H. Wang, F. Awai, R. Jono, M. M. Maitani, J. Nakazaki, T. Kubo, H. Segawa, *Nano Energy* **2018**, *45*, 184.

[32] D. J. Slotcavage, H. I. Karunadasa, M. D. McGehee, *ACS Energy Lett.* **2016**, *1*, 1199.

[33] E. T. Hoke, D. J. Slotcavage, E. R. Dohner, A. R. Bowring, H. I. Karunadasa, M. D. McGehee, *Chem. Sci.* **2015**, *6*, 613.

[34] H. Yuan, E. Debroye, K. Janssen, H. Naiki, C. Steuwe, G. Lu, M. Moris, E. Orgiu, H. Uji-i, F. D. Schryver, P. Samorì, J. Hofkens, M. Roeffaers, *J. Phys. Chem. Lett.* **2016**, *7*, 561.

[35] A. Merdasa, M. Bag, Y. Tian, E. Källman, A. Dobrovolsky, I. G. Scheblykin, *J. Phys. Chem. C* **2016**, *120*, 10711.

[36] D. Yang, W. Ming, H. Shi, L. Zhang, M.-H. Du, *Chem. Mater.* **2016**, *28*, 4349.

[37] Y. Yuan, J. Huang, *Acc. Chem. Res.* **2016**, *49*, 286.

[38] J. M. Frost, A. Walsh, *Acc. Chem. Res.* **2016**, *49*, 528.

[39] H. J. Snaith, A. Abate, J. M. Ball, G. E. Eperon, T. Leijtens, N. K. Noel, S. D. Stranks, J. T.-W. Wang, K. Wojciechowski, W. Zhang, *J. Phys. Chem. Lett.* **2014**, *5*, 1511.

[40] H. Yu, H. Lu, F. Xie, S. Zhou, N. Zhao, *Adv. Funct. Mater.* **2016**, *26*, 1411.

[41] P. Calado, A. M. Telford, D. Bryant, X. Li, J. Nelson, B. C. O'Regan, P. R. F. Barnes, *Nat. Commun.* **2016**, *7*, 13831.

[42] S. Meloni, T. Moehl, W. Tress, M. Franckevi̇us, M. Saliba, Y. H. Lee, P. Gao, M. K. Nazeeruddin, S. M. Zakeeruddin, U. Rothlisberger, M. Grätzel, *Nat. Commun.* **2016**, *7*, 10334.

[43] Z. Xiao, Y. Yuan, Y. Shao, Q. Wang, Q. Dong, C. Bi, P. Sharma, A. Gruverman, J. Huang, *Nat. Mater.* **2015**, *14*, 193.

[44] C. Eames, J. M. Frost, P. R. F. Barnes, B. C. O'Regan, A. Walsh, M. S. Islam, *Nat. Commun.* **2015**, *6*, 7497.

[45] C.-J. Tong, W. Geng, O. V. Prezhdo, L.-M. Liu, *ACS Energy Lett.* **2017**, *2*, 1997.

[46] J. M. Azpiroz, E. Mosconi, J. Bisquert, F. D. Angelis, *Energy Environ. Sci.* **2015**, *8*, 2118.

[47] J. Haruyama, K. Sodeyama, L. Han, Y. Tateyama, *J. Am. Chem. Soc.* **2015**, *137*, 10048.

[48] E. Tenuta, C. Zheng, O. Rubel, *Sci. Rep.* **2016**, *6*, 37654.

[49] A. Walsh, A. Zunger, *Nat. Mater.* **2017**, *16*, 964.

[50] E. H. Anaraki, A. Kermanpur, L. Steier, K. Domanski, T. Matsui, W. Tress, M. Saliba, A. Abate, M. Grätzel, A. Hagfeldt, J.-P. Correa-Baena, *Energy Environ. Sci.* **2016**, *9*, 3128.

[51] T. Duong, H. K. Mulmudi, H. Shen, Y. Wu, C. Barugkin, Y. O. Mayon, H. T. Nguyen, D. Macdonald, J. Peng, M. Lockrey, W. Li, Y.-B. Cheng, T. P. White, K. Weber, K. Catchpole, *Nano Energy* **2016**, *30*, 330.

[52] M. Zhang, J. S. Yun, Q. Ma, J. Zheng, C. F. J. Lau, X. Deng, J. Kim, D. Kim, J. Seidel, M. A. Green, S. Huang, A. W. Y. H.-Baillie, *ACS Energy Lett.* **2017**, *2*, 438.

[53] T. Duong, Y. Wu, H. Shen, J. Peng, X. Fu, D. Jacobs, E.-C. Wang, T. C. Kho, K. C. Fong, M. Stocks, E. Franklin, A. Blakers, N. Zin, K. McIntosh, W. Li, Y.-B. Cheng, T. P. White, K. Weber, K. Catchpole, *Adv. Energy Mater.* **2017**, *7*, 1700228.

[54] E. Mosconi, F. D. Angelis, *ACS Energy Lett.* **2016**, *1*, 182.

[55] B. C. O'Regan, P. R. F. Barnes, X. Li, C. Law, E. Palomares, J. M. Marin-Beloqui, *J. Am. Chem. Soc.* **2015**, *137*, 5087.

[56] W. Tress, N. Marinova, T. Moehl, S. M. Zakeeruddin, M. K. Nazeeruddin, M. Grätzel, *Energy Environ. Sci.* **2015**, *8*, 995.

[57] M. D. Bastiani, G. D.'Erba, M. Gandini, V. D'Innocenzo, S. Neutzner, A. R. S. Kandada, G. Grancini, M. Binda, M. Prato, J. M. Ball, M. Caironi, A. Petrozza, *Adv. Energy Mater.* **2016**, *6*, 1501453.

[58] Z. Li, C. Xiao, Y. Yang, S. P. Harvey, D. H. Kim, J. A. Christians, M. Yang, P. Schulz, S. U. Nanayakkara, C.-S. Jiang, J. M. Luther, J. J. Berry, M. C. Beard, M. M. A. -Jassima, K. Zhu, *Energy Environ. Sci.* **2017**, *10*, 1234.

[59] T. Bu, X. Liu, Y. Zhou, J. Yi, X. Huang, L. Luo, J. Xiao, Z. Ku, Y. Peng, F. Huang, Y.-B. Cheng, J. Zhong, *Energy Environ. Sci.* **2017**, *10*, 2509.

[60] S. v. Reenen, M. Kemerink, H. J. Snaith, *J. Phys. Chem. Lett.* **2015**, *6*, 3808.

[61] T. Zhang, M. Long, K. Yan, M. Qin, X. Lu, X. Zeng, C. M. Cheng, K. S. Wong, P. Liu, W. Xie, J. Xu, *Adv. Energy Mater.* **2017**, *7*, 1700118.

[62] W. J. Yin, T. Shi, Y. Yan, *Appl. Phys. Lett.* **2014**, *104*, 063903.

[63] J. Kim, S.-H. Lee, J. H. Lee, K.-H. Hong, *J. Phys. Chem. Lett.* **2014**, *5*, 1312.

[64] Q. Wang, Y. Shao, H. Xie, L. Lyu, X. Liu, Y. Gao, J. Huang, *Appl. Phys. Lett.* **2014**, *105*, 163508.

[65] Y. Lin, Y. Bai, Y. Fang, Q. Wang, Y. Deng, J. Huang, *ACS Energy Lett.* **2017**, *2*, 1571.

[66] W. Ke, G. Fang, Q. Liu, L. Xiong, P. Qin, H. Tao, J. Wang, H. Lei, B. Li, J. Wan, G. Yang, Y. Yan, *J. Am. Chem. Soc.* **2015**, *137*, 6730.

[67] J. P. Perdew, K. Burke, M. Ernzerhof, *Phys. Rev. Lett.* **1996**, *77*, 3865.

[68] G. Kresse, J. Hafner, *Phys. Rev. B* **1993**, *47*, 558.

[69] G. Kresse, J. Furthmüller, *Comput. Mater. Sci.* **1996**, *6*, 15.

[70] G. Kresse, J. Furthmüller, *Phys. Rev. B* **1996**, *54*, 11169.

[71] A. Tkatchenko, M. Scheffler, *Phys. Rev. Lett.* **2009**, *102*, 073005.

[72] G. Kresse, D. Joubert, *Phys. Rev. B* **1999**, *59*, 1758.

[73] G. Mills, H. Jonsson, G. K. Schenter, *Surf. Sci.* **1995**, *324*, 305.

[74] G. Henkelman, H. Jónsson, *J. Chem. Phys.* **2000**, *113*, 9978.

[75] G. Henkelman, B. P. Uberuaga, H. Jónsson, *J. Chem. Phys.* **2000**, *113*, 9901.